Iraqi Journal of Physics, 2025
https://doi.org/10.30723/ijp.v23i3.1509
Vol. 23, No.3, PP. 8-23
P-ISSN: 2070-4003
E-ISSN: 2664-5548

A Different Approach: the Role of Oxygen Isotope Polarity and Coupling Dynamics in Enhancing Sub-Barrier Fusion

Lina S. Abdalmajid[1] and Adil M. Hussein M. Saeed[1*]
[1]*Department of Physics, College of Science, University of Sulaimani, Sulaymaniyah, Iraq*
[*]Corresponding author: adel.hossien@univsul.edu.iq

Abstract
This work systematically investigates sub-barrier fusion enhancement in oxygen-induced reactions, highlighting the novel roles of projectile structure and coupled-channel dynamics. We demonstrate that the agreement between theoretical predictions and experimental data is significantly enhanced by considering multipole vibrations, multi-phonon excitations, and neutron transfer with negative *Q*-values, utilizing the BW 91 and AW 95 potentials. Unlike previous studies, this work explains isotope-dependent sub-barrier fusion enhancement across different mass regions by combining BW 91 and AW 95 potentials with multi-phonon excitations and negative *Q*-value neutron transfer channels. For the systems ^{16,18}O + ^{62}Ni, ^{116}Sn, and ^{208}Pb, fusion excitation functions and barrier distributions are calculated using Wong's formula and a modified CCFULL code. The neutron excess in ^{18}O facilitates specific negative *Q*-value neutron transfer channels, which contribute to lowering the fusion barrier and enhancing sub-barrier fusion. Barrier distribution analysis shows the crucial role of nuclear structure in determining the fusion probability landscape and serves as a benchmarking technique for assessing theoretical calculations. The ^{18}O + ^{116}Sn reaction resulted in a calculated cross-section value that was twice that of the ^{16}O + ^{116}Sn system. Similarly, the fusion cross-section of ^{18}O + ^{208}Pb is higher than that of ^{16}O + ^{208}Pb, and there is good agreement between the experimental peak and the corresponding barrier distribution as calculated by the three-point method. A similar rate was observed for the ^{18}O projectile, leading to a broadening energy width of the barrier distribution in comparison with the findings from the ^{16}O projectile.

Article Info.

Keywords:
Sub-Barrier Fusion Enhancement, Projectile Isotopes, Neutron Transfer, Modifying Coupled-Channel, Proximity (BW 91, AW 95).

Article history:
Received: Aug. 06, 2025
Revised: Aug. 17, 2025
Accepted: Aug. 22, 2025
Published: Sep.01, 2025

1. Introduction
In today's world, the fusion technique represents a promising global endeavor to attain clean energy. However, fusion reactions are the most challenging problem in heavy-ion processes since many of their characteristics are still undetermined [1]. Theoretical models are a valuable tool for studying fusion dynamics and the role of nuclear structure in reaction dynamics near the Coulomb barrier [2].

Heavy ion fusion reactions have undergone significant study over the past four decades [3-5]. The Wong model is used to calculate the fusion cross-section in the most basic description of nuclear fusion reactions and coupling dynamics. When the energy entering the fusion system is low, the reaction primarily occurs through quantum tunneling across the Coulomb barrier, resulting from the balance between the strong repulsive force and the attractive nuclear interaction [6]. In the tunneling case, the degree of freedom plays [7] a significant role in fusing nuclei. Accurate calculation of fusion cross-sections at sub-barrier energies requires incorporating the coupling effects of neutron transfer [8], vibrational [9], and rotational excitations, significantly improving the deformed fuse d nuclei cases [7, 10-12]. The principles behind the observed enhancement in fusion cross sections at sub-barrier energies above the one-dimensional

barrier penetration model calculations have been adequately explained using the coupled-channel method [5, 13]. Previous studies [14, 15] have shown how vibrational excitation modes [9], nucleon transfer channels [16], and static nuclear deformations [17] influence fusion [18-20].

Additionally, research has shown that in heavy-ion fusion, there is not just one fusion barrier but a range of them [21], which are influenced by the natural states of the nuclei, like their rotation and vibration. This range of barriers is known as the fusion barrier distribution, and the colliding nuclei's structural characteristics significantly impact its shape [22, 23]. Couplings to inelastic and transfer channels are frequently considered in theoretical models using coupled-channel calculations [21, 24]. Rowley et al.[22] demonstrated that the energy distribution of a discrete spectrum of barriers might be calculated under specific approximations from exact fusion cross-sections by calculating the second derivative of the quantity ($\mathrm{E}_{c.m.}\sigma$) concerning the center-of-mass energy $E_{c.m.}$. This distribution [22] shows the influence of nuclear structure on the fusion process.

Understanding the puzzling behavior of heavy-ion fusion events has fundamentally necessitated an optimal choice of the nucleus-nucleus potential due to the considerable uncertainties in the radial dependence of the nuclear potential [16]. Various nuclear potentials, such as Woods-Saxon Potential, Proximity Potential, AW 95, BW 91, CW 76, etc., are available for this purpose [25]. The Woods-Saxon version of the nuclear potential has been utilized to describe the mechanism of heavy-ion reactions and is typically employed in coupled channel models. The three parameters of the static Woods-Saxon potential-depth (V_0), diffuseness (a_0), and range (r_0) - are inherently related to one another. Numerous issues related to the dynamics of heavy-ion fusion can be effectively resolved by considering the multifaceted nature of nucleus-nucleus potentials. There is much more to learn about the nuclear interaction component. Understanding the critical function of nuclear potential is essential to studying fusion processes. Interestingly, according to the well-known Wong formula, the nuclear potential controls both the potential's shape and the Coulomb barrier's height [26]. Several theoretical methods have been proposed to determine and explain the nuclear potential between two colliding nuclei.

Previous studies observed variations in sub-barrier fusion enhancement across different isotopic fusion systems, but a clear link between fusion enhancement order and inherent nuclear degrees of freedom has not been established. In order to address this gap, the current study investigates the fusion cross-sections of ^{16}O and ^{18}O projectiles with target nuclei ^{62}Ni, ^{116}Sn, and ^{208}Pb using the BW 91 and AW 95 potentials inside Wong's formula and CCFULL program. This allows us to investigate how isotope polarity and coupling dynamics contribute to an enhancement of sub-barrier fusion in medium, and heavy mass regions.

The aim of this work is to systematically investigate the effects of projectile isotope composition and coupled-channel dynamics−including multi-phonon excitations and neutron transfer with negative *Q*-values−on sub-barrier fusion cross sections. Using BW 91 and AW 95 proximity potentials within Wong's formula and a modified CCFULL code, we study fusion reactions of ^{16,18}O with ^{62}Ni, ^{116}Sn, and ^{208}Pb to understand the interplay of nuclear structure and coupling effects across different mass regions. This study seeks to clarify the role of nuclear potential choice and coupling mechanisms in enhancing fusion probabilities below the Coulomb barrier.

2. Theoretical Formalism

2.1 Potentials

The Broglia and Winther 1991 (BW 91) and Aage Winther (AW 95) potentials were used in Wong's formula and coupled-channel equation through a modified CCFULL code.

2.1.1 Broglia And Winther 1991 (BW 91)

Broglia and Winther [27] developed a modified version of the aforementioned potential using Woods-Saxon parametrization. This potential to be as [28]

$$V_N^{BW91}(r) = -\frac{V_0}{1+\exp\left(\frac{r-R_0}{0.63}\right)} \text{ MeV}, \quad \textbf{(1)}$$

where V_0 is the potential depth, R_0 is the fused radius, and a is the diffuseness parameter. In the BW 91 parametrization, the diffuseness is fixed at $a = 0.63$ fm.

The potential depth given by

$$V_0 = 16\pi \frac{R_1 R_2}{R_1+R_2}\gamma a, \quad \textbf{(2)}$$

and

$$\mathrm{R_0 = R_1 + R_2 + 0.29} \quad \textbf{(3)}$$

Here nucleus radius R_i has the form

$$R_i = 1.233A_i^{1/3} - 0.98A_i^{-1/3} \text{ fm } (i = 1,2) \quad \textbf{(4)}$$

and the surface energy coefficient is expressed as

$$\gamma = \gamma_0 \left[1 - k_s \left(\frac{N_p - Z_p}{A_p}\right)\left(\frac{N_t - Z_t}{A_t}\right)\right] \quad \textbf{(5)}$$

where $k_s = 1.8$ and $\gamma_0 = 0.95$ MeV/ fm^2.

It should be noted that when the projectile is symmetric (N = Z) and the target is asymmetric (N > Z), the second term of the γ distinct outcomes.

2.1.2 Aage Winther (AW 95)

After thoroughly comparing with experimental data for heavy-ion elastic scattering, Winther modified the parameters of the mentioned potential. This fine-tuning to slightly altered the diffuseness parameter " a " and the nuclear radius R_i values [28, 29]

$$a = \left[\frac{1}{1.17\left(1+0.53\left(A_1^{-1/3}+A_2^{-1/3}\right)\right)}\right] \text{ fm} \quad \textbf{(6)}$$

and

$$R_i = 1.20A_i^{1/3} - 0.09 \text{ fm } (i = 1,2) \quad \textbf{(7)}$$

here $R_0 = R_1 + R_2$ only, this potential was assigned the name AW 95.

2.2 One-Dimensional Wong's Formula

The experimental finding is well explained by the barrier penetration model created by Wong [26, 30], which has been frequently used to characterize the fusion cross sections, especially at energies above the Coulomb barrier. The Coulomb potential

($V_C(r)$) and nuclear proximity potential ($V_N(r)$) combine to form the total potential ($V_T(r)$).

$$V_T(r) = V_N(r) + V_C(r), \quad \text{where } V_C(r) = \frac{Z_1 Z_2 e^2}{r} \tag{8}$$

The calculated barrier height V_B^{th} and its position R_B^{th} can be determined using the provided formula and boundary conditions, $\left.\frac{dV_T(r)}{dr}\right|_{r=R_B^{th}} = 0$, and $\left.\frac{d^2V_T(r)}{dr^2}\right|_{r=R_B^{th}} \leq 0$.

Using Wong's model [28, 31] to calculate the fusion cross-section, which is expressed as:

$$\sigma_{fus} = \frac{\pi}{k^2}\sum_{l=0}^{l_{max}}(2l+1)T_l(E_{c.m.}) \tag{9}$$

The wave number, k, is defined as $\sqrt{\frac{2\mu E_{c.m.}}{\hbar^2}}$, where μ is the reduced mass and $E_{c.m.}$ denotes the center-of-mass energy. The formula above uses l_{max}, the most significant partial wave exhibiting a pocket within the interaction potential, and $T_l(E_{c.m.})$ represents the penetrating probability, which plays as the energy-dependent barrier penetration factor, which is:

$$T_l(E_{c.m.}) = \left\{1 + \exp\left[\frac{2\pi}{\hbar\omega_l}(V_B^{th} - E_{c.m.})\right]\right\}^{-1} \tag{10}$$

Where $\hbar\omega_l$ is the curvature of the inverted parabola. With width and barrier position independent on orbital angular momentum l, the fusion cross section becomes

$$\sigma_{fus}(mb) = \frac{10\,R_B^{th^2}\hbar\omega_0}{2\,E_{c.m.}} \ln\left\{1 + \exp\left[\frac{2\pi}{\hbar\omega_l}\left(E_{c.m.} - V_B^{th}\right)\right]\right\} \tag{11}$$

when $E_{c.m.} \gg V_B^{th}$, the formula simplifies to the used sharp cut-off formula.

$$\sigma_{fus}(mb) = 10\,\pi\,R_B^{th^2}\left(1 - \frac{V_B^{th}}{E_{c.m.}}\right) \tag{12}$$

whereas for $E_{c.m.} \ll V_B^{th}$, the formula (11) transforms, and the parameter of ($\hbar\omega_0 \backsimeq \hbar\omega_B$) is the curvature of the inverted parabola. A description of the very low-energy fusion cross-section behavior near and below the Coulomb barrier can be obtained.

$$\hbar\omega_B = \left[\frac{-\hbar^2}{\mu}\left.\frac{d^2V_T(r)}{dr^2}\right|_{r=R_B^{th}}\right]^{1/2}$$

with width and barrier location dependent the fusion cross section becomes,

$$\sigma_{fus}(mb) = \frac{10R_B^{th^2}\hbar\omega_0}{2\,E_{c.m.}}\exp\left[\frac{2\pi}{\hbar\omega_0}(E_{c.m.} - V_B^{th})\right] \tag{13}$$

We used the equation above to calculate the cross-section of the fusion.

2.3 Coupled-Channel Equations

The second method for calculating the fusion cross-section is the coupled channel analysis, which indicates the influences of inelastic surface excitations and multi-neutron transfer channels with ground-state *Q*-values on the fusion process [6].

$$\left[-\frac{\hbar^2}{2\mu}\frac{d^2}{dr^2} + \frac{J(J+1)\hbar^2}{2\mu r^2} + V_N^0(r) + \frac{Z_P Z_T e^2}{r} + \epsilon_n - E\right]\psi_n(r) + \sum_m V_{nm}(r)\,\psi_m(r) = 0 \tag{14}$$

The relative motion distance between the projectile and target is denoted by r, and the reduced mass is denoted by μ. E is the bombarding energy in the center of mass frame, and ϵ_n is the n_{th} channel's excitation energy. The coupling Hamiltonian's matrix elements, V_{nm}, are made up of nuclear and Coulomb components in the collective model.

We use a Woods-Saxon potential to represent the nuclear potential (V_N^0) of the entrance channel. Our code uses a potential that can be parameterized as either BW 91 or AW 95, as defined before, which is given as [6].

$$V_N^0(r) = -\frac{V_0}{1+\exp\left(\frac{r-R_0}{a}\right)} \quad \textbf{(15)}$$

The fusion cross section is computed by,

$$\sigma_{fus}(E) = \sum_J \sigma_J(E) = \frac{\pi}{k_0^2}\sum_J (2J+1)\, P_J(E) \quad \textbf{(16)}$$

Where the detail of cross-section probability $P_J(E)$ can be found in [6, 12] and k_0 is the wave number for $l_{th} = 0$.

2.4 Theoretical Method of the Fusion Barrier Distribution

Heavy-ion fusion research has advanced significantly with fusion barrier distribution measurements. They offer an effective way to comprehend the role of intrinsic degrees of freedom and the fusion mechanism. Recently, an analytical technique has been suggested to extract this distribution directly from fusion data [32]. Analyzing the distribution of barriers gives a deeper understanding of reaction dynamics, sub-barrier fusion, and the crucial role of channel couplings (often ignored in single-barrier models). The distribution of barriers from fusion cross-section data, $D_f(E)$ can be extracted using the second derivative method:

$$D_f(E) = \frac{d^2(E\sigma)}{dE^2} \quad \textbf{(17)}$$

Where $D_f(E)$ is the fusion barrier distribution, E is the center of mass energy in MeV, and σ is the fusion cross-section at energy E. Nearly all barrier distribution calculations depend on the three-point difference formula provided by [33] to compute the second derivative:

$$\frac{d^2(E\sigma)}{dE^2} = 2\left(\frac{(E\sigma)_3-(E\sigma)_2}{E_3-E_2} - \frac{(E\sigma)_2-(E\sigma)_1}{E_2-E_1}\right)\left(\frac{1}{E_3-E_1}\right). \quad \textbf{(18)}$$

This is computed at energy $(E_1 + 2E_2 + E_3)/4$ and roughly takes the following form for energy data that are evenly spaced [23, 32].

$$\frac{d^2(E\sigma)}{dE^2} = \left(\frac{(E\sigma)_3-2(E\sigma)_2+(E\sigma)_1}{\Delta E^2}\right) \quad \textbf{(19)}$$

The second method is model-based, in which Wong's formula, an analytical expression derived from a one-dimensional barrier penetration model, is used to match the experimental fusion cross-sections. The theoretical barrier distribution is obtained by analytical calculation on the second derivative of Wong's function (Eq.13) following fitting [32].

$$\frac{d^2(E\sigma)}{dE^2} = \frac{2\pi^2 R_B^2}{\hbar\omega_B}\frac{\exp(x)}{(1+\exp(x))^2} \quad \textbf{(20)}$$

Where $x = 2\pi(E - V_B)/\,\hbar\omega_B$

We are using the experimental data and the effect of coupling to validate the two approaches. We use these methods to find the fusion barrier distribution from the experimental and theoretical fusion cross-section data. The second method employed a least-squares optimization methodology to fit Wong's formula (Eq. 13) by using the experimental and theoretical (CCFULL) fusion cross-sections. Following the fitting process, the optimized barrier parameters (as shown in Tables 3 and 5) are used in Eq. 20

to calculate the corresponding barrier distribution. The first technique used the regular three-point finite difference formula (Eq. 18) on the theoretical fusion cross-sections calculated with CCFULL. It is essential to note that all excitation states and neutron transfer cases used to set the CCFULL code parameters for calculating the cross-section value are identical to those used for calculating the barrier distribution value. Additionally, we note these cases in the figure's margins. Fig.1 shows the diagrammatic representation of the theoretical models that used in calculation.

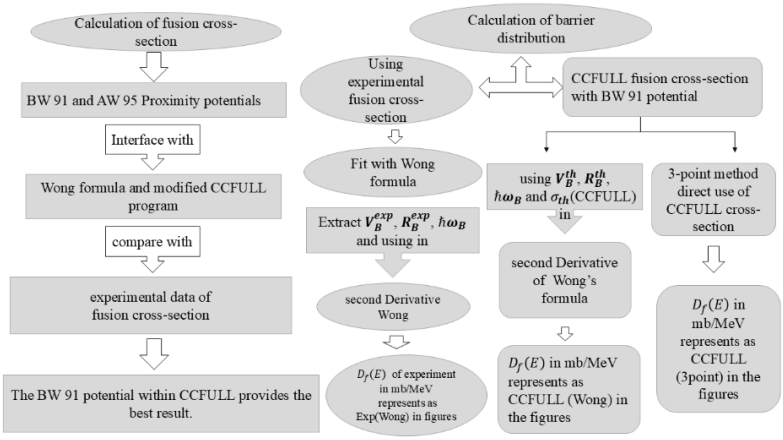

Figure 1: Diagrammatic representation of the theoretical models that used in calculation.

3. Results and Discussions of Cross -Section

The present study employs various potentials to calculate the fusion cross-section. The Wong formula, using the Hill–Wheeler approach, applied the two proximity potentials (BW 91 and AW 95) separately to match the experimental data on fusion cross-sections, particularly at high energy levels. Conversely, because the theoretical Wong model ignores couplings to nuclear structure effects like inelastic excitations and neutron transfer channels, it is unable to replicate the experimental fusion cross-section at low energy across all reactions, as shown in the figures discussed later. To address this issue, we implement the AW 95 and BW 91 potentials in the CCFULL program to provide the optimal value for the cross-section because the coupled channel method based on coupling between relative motion and intrinsic degrees of freedom of fusing nuclei, which Wong's formula does not consider [16]. In addition, the coupling was investigated using two different excitation energy levels as input information for the CCFULL code. If required, we enter the vibration/rotation mode according to the characteristic of fused nuclei to the CCFULL code. In addition, we take into account the neutron transfer and *Q*-value during the fusion cross-section calculation of the aforementioned systems. Table 1 lists the completeness parameters for the CCFULL calculation, including the values for the deformation parameters (β_λ) and the excitation energies (E_λ) associated with the low-lying vibration states of all these nuclei. The best agreement between the theoretical and actual fusion cross-sections was obtained by manually adjusting the transfer coupling strength, F_t. Neutron transfer effects on sub-barrier fusion are reasonably described by the selected value, which is consistent with similar systems.

The optimized transfer coupling strength is F_t= 0.3 MeV, reproducing the experimental data for some of the fusion systems. All these code adjustments are used for two methods: to calculate the fusion cross-section for the oxygen nucleus and its isotopes when they act as projectiles in the fusion systems ^{16,18}O + ^{62}Ni, ^{16,18}O + ^{116}Sn and ^{16,18}O + ^{208}Pb and to enhance the fusion reaction, which is discussed in the subsection below based on the projectile's isotopes. While previous research [8, 15, 25] showed a general fusion enhancement in O-induced systems, they did not specifically attribute this impact

to multi-phonon excitations or negative *Q*-value transfer channels. In contrast, our analysis demonstrates that these transfer couplings are necessary to replicate the experimental findings when combined with multi-phonon excitations. In contrast to earlier research that concentrated on individual targets or just on vibrational excitations, our analysis offers a systematic isotope-dependent comparison of medium, and heavy targets.

Table 1: The deformation parameters β_λ and their corresponding excitation energies (E_λ) for the 2^+, 3^- and 5^- vibrational states of the reaction partners.

Nucleus	β_2	E_2 (MeV)	β_3	E_3 (MeV)	β_5	E_5 (MeV)	References
^{16}O	0.362	6.92	0.79	6.13	--	--	[34, 35]
^{18}O	0.355	1.982	0.390	5.098	--	--	[34]
^{62}Ni	0.198	1.173	0.220	3.757	--	--	[34]
^{116}Sn	0.143	1.293	0.213	2.266	--	--	[2, 35]
^{208}Pb	0.054	4.086	0.161	2.615	0.056	3.198	[36-39]

3.1 ^{16,18}O + ^{62}Ni

The double magic projectile ^{16}O and the magic target nucleus ^{62}Ni fused to form the ^{16}O + ^{62}Ni system. Fig. 2(a, b) displays the calculated fusion cross-sections for the two systems (^{16,18}O + ^{62}Ni). The theoretical calculations are close to the experimental data. In particular, the BW 91 and AW 95 potentials have been integrated into the CCFULL program, which is influenced by the deformation parameter outlined in Table 1. The result is reproducing the experimental fusion cross-sections at low energy of the fusion cross-sections in the sub-barrier area.

In the ^{16}O + ^{62}Ni system, to accurately reproduce the experimental fusion results requires more than just using the projectile's 2^+ and 3^-vibrational states, as shown in Fig. 2(a). After accounting for projectile vibrational states, we coupled it with the target's one-phonon in 2^+ and 3^- vibrational states. However, the number of phonons played a role in the improvement. Having more phonon vibrational states in the target affects the results, increasing the fusion cross-section and causing a significant difference from the experimental results [16]. In addition, the neutron transfer channel (1-neutron pickup) with a negative *Q*-value equal to -6.230 MeV with the transfer coupling strength F_t = 0.3 MeV.

The projectile's non-closed shell structure for neutrons in the ^{18}O + ^{62}Ni system is expected to significantly impact the fusion dynamics, and the theoretical calculations successfully predicted the experimental results (see Fig. 2(b)). Predictions based on the interaction of two phonons in the target's 2^+ vibrational states are included in the CCFULL calculations. Two neutrons are transferred (pickup) with a negative *Q*-value of -6.852 MeV with F_t = 0.3 MeV.

Fig. 2(c, d) shows a minor enhancement in the ^{18}O + ^{62}Ni cross-section because of its lower barrier height (30.90 MeV; see Table 3), which marginally raises the fusion probability at higher $E_{c.m.}$. Since the sub-barrier dynamics is dominated by vibrational couplings and the negative *Q*-value transfer channels are either weak or energetically unfavorable, the two extra neutrons in ^{18}O have a minimal impact in this system.

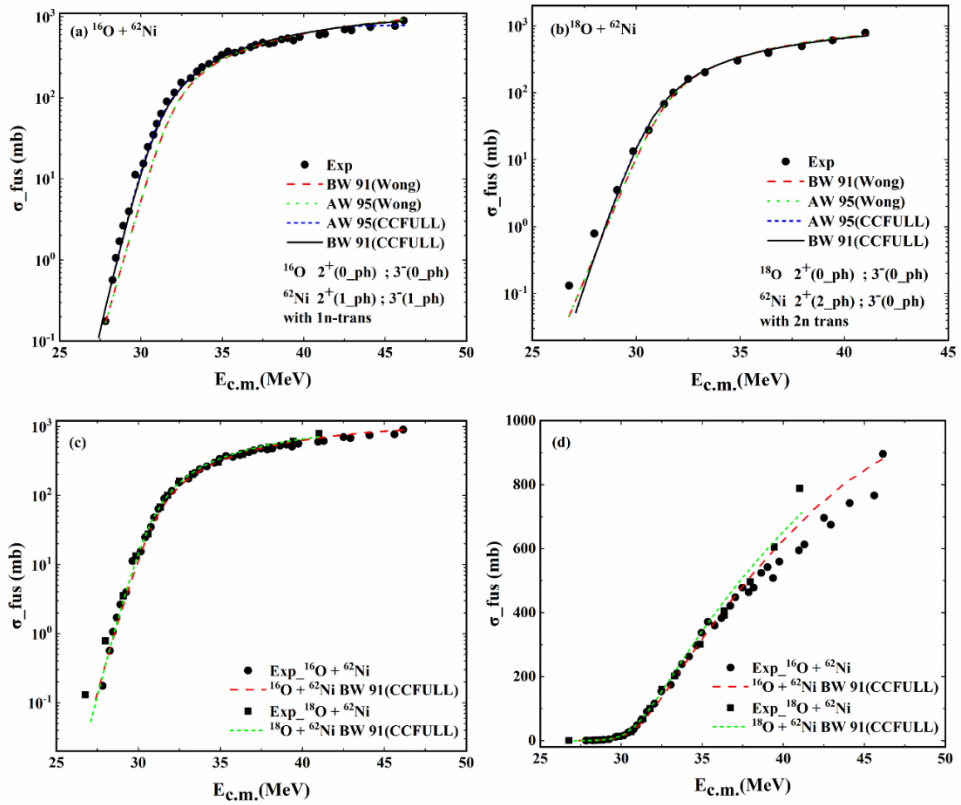

Figure 2: Fusion excitation functions (cross-sections) for the ^{16,18}O + ^{62}Ni systems calculated using the BW 91 and AW 95 proximity potentials within Wong's formula and coupled-channels model (CCFULL code). Results show in (a) ^{16}O + ^{62}Ni and (b) ^{18}O + ^{62}Ni. Comparisons between the two projectiles (^{16}O and ^{18}O) with the same ^{62}Ni target are presented in (c) logarithmic and (d) linear scales. The experimental data come from Ref [39, 40].

3.2 ^{16,18}O + ^{116}Sn

Fig. 3 illustrates that the ^{16,18}O + ^{116}Sn systems are suitable for the fusion enhancement below the barrier energy, considering the target's vibration states of type $2^+$and 3^-. These states are used as input parameters for the CCFULL when compared with the Wong formula. Fig. 3(a) shows the enhancement of the CCFULL-calculated fusion of ^{16}O + ^{116}Sn using vibration modes and the phonon number, which coincides with experimental data compared to Wong's formula. The improved CCFULL results are influenced by specific conditions, including the two-phonon states of types $2^+$and 3^- in the target and the one-phonon and two-phonons $2^+$and 3^- vibrational states in the projectile. Table 1 presents the deformation parameters corresponding to the multipolarities of the vibrational states. Tables 2 and 3 provide the obtained values of the parameters characterizing the nuclear potentials and Coulomb barrier parameters employed in the calculations.

Tripathi et al.[35] mentioned that adding a single phonon in 2^+ or 3^- vibrational coupled states improved the calculated fusion cross sections for the ^{16}O + ^{116}Sn system. However, their model still did not accurately reproduce the experimental data. In addition, other previous studies highlighted the role of projectile and target vibrational states in ^{16}O + ^{116}Sn in understanding fusion dynamics. Gautam [41] showed that one-phonon in 3^- and two-phonon in $2^+$are sufficient in the coupled-channel structure. Thereby, V. Ghanghas et al. [16] analyzed experimental data by parametrizing the Wood-Saxon potential related to coupled-channel calculations, using double phonon of vibrational 2^+or 3^- states of ^{116}Sn. Their approach is also lacking in the high energy $E_{c.m.}$ range, with findings that deviate significantly from experimental data.

Our study resolves this issue, presenting results that align more closely with high-energy measurements. We used our models to test with a different projectile fusion. Consistently using the ^{116}Sn target and oxygen isotope ^{18}O. In Fig. 3(b) for the ^{18}O + ^{116}Sn system, we discovered that using the two-phonon in the 3^- state of the target and the two-phonon in the 2^+ state for the projectile provides the best approach to the experimental data. Further, since the quadrupole excitation energy in the projectile (^{18}O) lies at a much lower energy than those in the projectile (^{16}O), as Table 1 illustrates, they are expected to have a major role in the fusion process of the selected system.

It is important to note that the effect of channel coupling gets stronger when the ratio of neutrons to protons (N/Z) increases; this is more evident in ^{18}O + ^{116}Sn reactions. At a higher value of the $E_{c.m.}$, the probability of fusion occurring for the ^{18}O + ^{116}Sn system is twice as much as for the ^{16}O + ^{116}Sn system, as shown in Fig. 3(d). In addition, one neutron transfer channel with a negative *Q*-value of -1.102 MeV (Table 4) was linked to an increase in sub-barrier fusion for the ^{18}O + ^{116}Sn system compared to the ^{16}O + ^{116}Sn system, as shown in Fig. 2(d) [42]. While Nabendu Kumar Deb et al. [43], Vijay Ghanghas et al. [16, 35], and others reported that negative *Q*-values do not affect enhancement. The calculations of fusion barrier parameters for these systems are shown in Table 3. Another factor contributing to this rise is the high excitation energies of 2^+ and 3^- in ^{16}O, which are 6.92 MeV and 6.13 MeV, respectively, in contrast to their values in ^{18}O, which are 1.982 MeV and 5.098 MeV. The combined effect of lower projectile excitation energies and the availability of a negative *Q*-value neutron transfer channels, which increases tunneling probability, results in an enhancement of sub-barrier fusion in ^{18}O + ^{116}Sn as compared to ^{16}O + ^{116}Sn. As a result of these parameters along with two-phonon excitations in both the projectile and target vibrational states, the ^{18}O system achieves nearly double the fusion probability at higher $E_{c.m.}$ than the ^{16}O system.

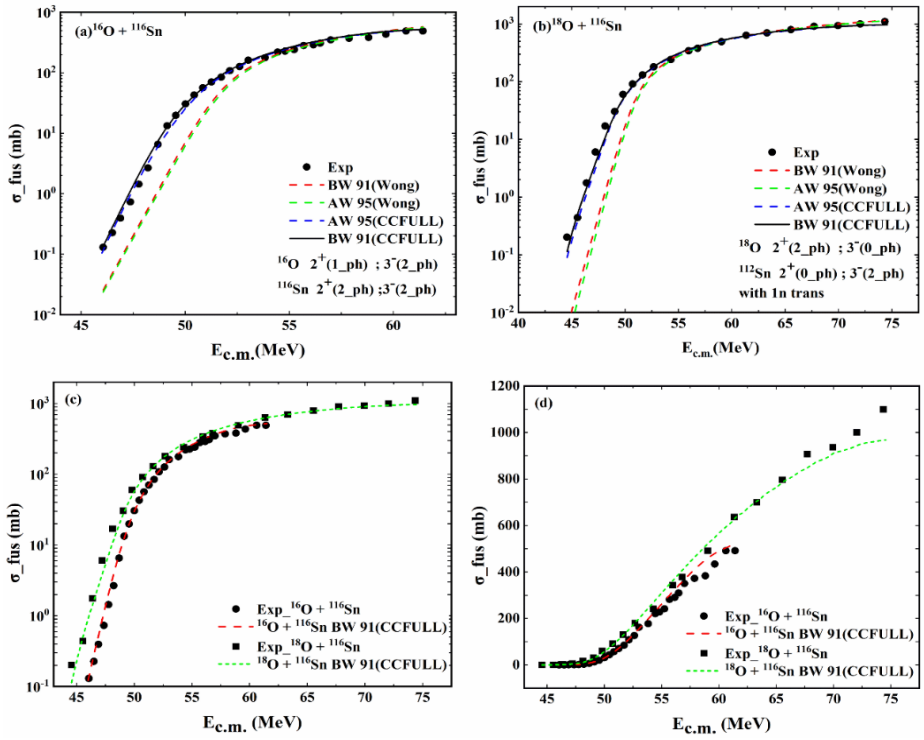

Figure 3: Fusion excitation functions (cross-sections) for the ^{16,18}O + ^{116}Sn systems calculated using the BW 91 and AW 95 proximity potentials within Wong's formula and coupled-channels model (CCFULL code). Results show in (a) ^{16}O + ^{116}Sn and (b) ^{18}O + ^{116}Sn. Comparisons between the two projectiles (^{16}O and ^{18}O) with the same ^{116}Sn target are resented in (c) logarithmic and (d) linear scales. The experimental data come from Ref [2, 39].

3.3 ^{16,18}O + ^{208}Pb

Fig. 4(a) shows the fusion cross-sections for the ^{16}O + ^{208}Pb reaction. Both the projectile and target are doubly magic nuclei with spherical forms. Wong formula calculation based on both nuclear potentials, fails to reproduce experimental fusion cross-sections in the sub-barrier energy region. The BW 91 potential in combination with CCFULL code, properly addresses this sub-barrier fusion behavior by including couplings to two-phonon excitations in the 2^+ and 3^- vibrational states of ^{16}O and 3^- and 5^- for ^{208}Pb, with a one-neutron transfer (stripping) channel with a negative *Q*-value of -11.726 MeV with F_t = 0.3 MeV [42].

On the other hand, in the fusion of ^{18}O + ^{208}Pb the coupling to one phonon in 3^- vibrational states of target and four phonons in 2^+ vibrational state of projectile gives the best agreement fusion cross-section with experiment data with one-neutron transfer (pickup) reaction of *Q*-value equal to -3.412 MeV and F_t = 0.3 MeV. The barrier parameters for these reactions are listed in Table 3. On can conclude that, the ^{18}O projectile can reduce the negative *Q*-value. Fig. 4(c, d) illustrates this process. There is a fusion enhancement between these two systems; ^{18}O + ^{208}Pb exhibits a higher fusion cross-section than ^{16}O + ^{208}Pb. It could be due to the double-magic nature of both the projectile and the target in ^{16}O + ^{208}Pb. Additionally, the fusion system ^{18}O + ^{208}Pb is more likely to occur, as the ^{18}O target possesses two neutrons outside its stable shell. These two neutrons are more likely to engage in the reaction, while the higher energy level of ^{16}O compared to ^{18}O, complicates nucleon transfer, ultimately reducing the fusion cross-section. The two additional neutrons in ^{18}O, with lower negative *Q*-value neutron transfer channels and pair well with multi-phonon excitations in both the projectile and the target, are specifically responsible for the greater sub-barrier fusion cross-section in ^{18}O + ^{208}Pb as opposed to ^{16}O + ^{208}Pb. On the other hand, the doubly magic ^{16}O + ^{208}Pb combination has fewer available channels and higher negative *Q*-values, which limit nucleon transfer. Additionally, vibrational couplings by themselves cannot increase the fusion cross-section. Future research on heavier nuclei, superheavy element synthesis, and neutron-rich projectile effects can be guided by our findings on multi-phonon excitations and negative *Q*-value neutron transfers in ^{18}O-induced fusion.

Table 2: Nuclear potential parameters are used for the studied reactions in the CCFULL code.

Reactions	BW 91			AW 95		
	V_0 (MeV)	R_0 (fm)	a_0 (fm)	V_0 (MeV)	R_0 (fm)	a_0 (fm)
^{16}O + ^{62}Ni	51.53	7.64	0.63	54.66	7.59	0.64
^{18}O + ^{62}Ni	52.14	7.78	0.63	55.27	7.71	0.64
^{16}O + ^{116}Sn	55.72	8.82	0.63	60.15	8.70	0.65
^{18}O + ^{116}Sn	56.04	8.96	0.63	60.44	8.82	0.65
^{16}O + ^{208}Pb	59.22	10.15	0.63	64.97	9.95	0.66
^{18}O + ^{208}Pb	58.80	10.29	0.63	64.41	10.07	0.66

Table 3: Coulomb barrier parameters are used in the CCFULL code for the studied reactions.

Reactions	BW 91			AW 95		
	V_B^{th} (MeV)	R_B^{th} (fm)	$\hbar\omega_B$ (MeV)	V_B^{th} (MeV)	R_B^{th} (fm)	$\hbar\omega_B$ (MeV)
^{16}O + ^{62}Ni	31.41	9.56	3.77	31.38	9.57	3.76
^{18}O + ^{62}Ni	30.90	9.73	3.55	30.89	9.73	3.53
^{16}O + ^{116}Sn	51.25	10.25	4.29	51.37	10.48	4.25
^{18}O + ^{116}Sn	50.52	10.69	4.03	50.67	10.63	3.98
^{16}O + ^{208}Pb	76.11	11.69	4.74	76.54	11.59	4.68
^{18}O + ^{208}Pb	75.19	11.84	4.44	75.67	11.72	4.37

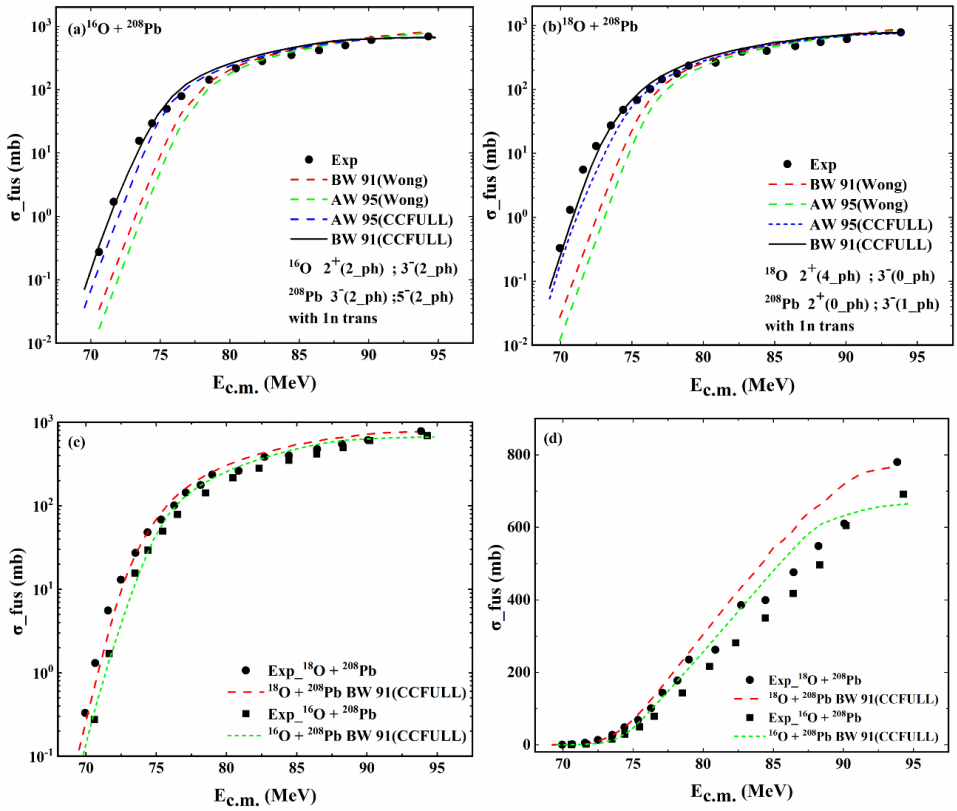

Figure 4: Fusion excitation functions (cross-sections) for the $^{16,18}O + ^{208}Pb$ systems calculated using the BW 91 and AW 95 proximity potentials within Wong's formula and coupled-channels model (CCFULL code). Results show in (a) $^{16}O + ^{208}Pb$ and (b) $^{18}O + ^{208}Pb$. Comparisons between the two projectiles (^{16}O and ^{18}O) with the same ^{208}Pb target are presented in (c) logarithmic and (d) linear scales. The experimental data are come from Ref [39, 44].

Table 4: Q-values in (MeV) for ground-state neutron transfer, where Q_{-1n} denotes neutron stripping and Q_{+1n} and Q_{+2n} indicate neutron pickup by the projectile.

Reactions	Q_{-1n}	Q_{+1n}	Q_{+2n}	references
$^{16}O + ^{62}Ni$	--	-6.230	--	[34]
$^{18}O + ^{62}Ni$	--	--	-6.852	[40]
$^{16}O + ^{116}Sn$	--	--	--	--
$^{18}O + ^{116}Sn$	-1.102	--	--	[16]
$^{16}O + ^{208}Pb$	-11.726	--	--	[42]
$^{18}O + ^{208}Pb$	--	-3.412	--	[42]

4. Results of the Fusion Barrier Distribution

Fig. 5(a) shows the barrier distribution for the $^{16}O + ^{62}Ni$ system. A single peak appears in the experimental barrier distribution with width ranging from 27 to 35.5 MeV. The dashed curve (3-point) method comes directly from the cross-section calculated by the CCFULL code, which can recreate the main peak with a low strength rate. However, it displays additional erroneous peaks at higher energies ($E_{c.m.} \geq 37.5$ MeV). These could be caused by limitations in the numerical instabilities inherent in the finite-difference method. To address the additional erroneous peaks identified in the 3-point method, we implemented an alternative approach based on Wong's formula. The red curve is obtained using Wong's second derivative method, with barrier parameters extracted from the modified CCFULL code, closely matches the main peak of the experimental data, ignoring the heights of the peaks. This consistent performance indicates that the CCFULL

model effectively combines the coupling channels defined by the couplings to the 2^+ and 3^- vibration states of the ^{62}Ni target using 1-phonon; additionally, the one-neutron transfer with a *Q*-value of -6.230 MeV is crucial for reproducing the experimental peak.

As mentioned, we replaced the projectile oxygen by its isotope (^{18}O) to enhance the reaction. Fig. 5(b) illustrates the barrier distribution of ^{18}O + ^{62}Ni. It is noteworthy that the experimental data exhibit a broad range of coupling values, specifically from 26 to 40 MeV, when compared to ^{16}O + ^{62}Ni. Both the theoretical calculation CCFULL (solid line) and the 3-point method (dashed curve) are able to replicate the experimental results, but they shifted a narrower peak to the right. The 3-point method indicates that collective excitation energies and deformation parameters are essential for understanding the reaction. A coupling worked with 2-phonon for the 2^+ state of ^{62}Ni (see Fig. 5(b)), and a two-neutron transfer with a *Q*-value of -6.852 MeV.

In the Fig. 5(c), the experimental barrier distribution for the ^{16}O + ^{116}Sn system displays a prominent, symmetric peak around $E_{c.m.}\approx$ 50 MeV. The solid line replicates the peak's position, in addition the solid line better matches the experimental distribution's width and position, suggesting strong channel coupling as shown in the figure. To replicate the experimental barrier distribution, the 2^+ and 3^- states of both ^{16}O and ^{116}Sn were used. Furthermore, the experimental barrier distribution (black dots) for ^{18}O + ^{116}Sn in Fig. 5(d) has curves smoothly and bell-shapely, culminating at $E_{c.m.}$= 43-58 MeV at about ($D_f(E)$ =522 mb/MeV), which achieved a broader coupling region if compared with the ^{16}O + ^{116}Sn. Both theoretical calculations repeat the same setting but with different number of phonons and one neutron transfer in ^{18}O + ^{116}Sn. The solid red line from the Wong models indicates a trend that adjusts to ($E_{c.m.}$= 45–55) MeV, exhibiting a sharper drop while predicting a higher peak ($D_f(E)$ > 1200 mb/MeV) and shifting the main peak toward the right of experimental barriers peak. This behavior is attributed to the neutron transfer effect with a *Q*-value of -1.102 MeV. Furthermore, the dashed line (3-point) does not successfully replicate the experimental main peak, as it displays several ripples as pileup main peak, and several wave in the higher energy region.

The fusion barrier distribution for the ^{16}O + ^{208}Pb system is shown in Fig. 5(e). The experimental distribution (black dots) shows a smooth and huge strength peak, centered near $E_{c.m.}$=76.1 MeV. The theoretical curve by Wong model (solid line) shows a much sharper and narrower peak that has shifted to a lower energy level, peaking around $E_{c.m.}$=73.6 MeV, which is overestimated and much higher than what the experimental data shows. Wong's model clearly falls short in explaining the experimental data. Therefore, the 3-point model aims to reproduce accurately the centroid and breadth of the experimental peak, as represented by the solid line. The main peak can be recreated toward the low energy potion by using a suitable set of parameters that includes the 2-phonon excitation states 3^- and 5^- of ^{208}Pb, and the 2^+ and 3^- states of ^{16}O, along with a one-neutron transfer that has a *Q*-value of -11.726 MeV. The extra phonon transition causes an additional peak at high energy [21].

The Oxygen projectile ^{18}O always plays as a corrector for these fusion systems. The experiment barrier distribution for the ^{18}O + ^{208}Pb system is centered around $E_{c.m.}\approx$ 75 MeV, as shown in Fig. 5(f). The red solid line shows that, based on Wong's calculation, the barrier strength shifts to the right of the experimental peak, which is usually a low-energy area centered on $E_{c.m.}\approx$ 73.5 MeV. The dashed curve aligns with the experimental data, attempting to match the peak width observed in the experiments. We chose the multipolarities and phonon numbers of the excited vibrational state that corresponded to the deformed projectile ^{18}O and the self-excited target ^{208}Pb, which are different from the vibrational states of the ^{16}O + ^{208}Pb system. We successfully reproduced the experimental peak, as depicted in Fig. 5(f). Therefore, multipolarity and phonon numbers have an important role in this optimization.

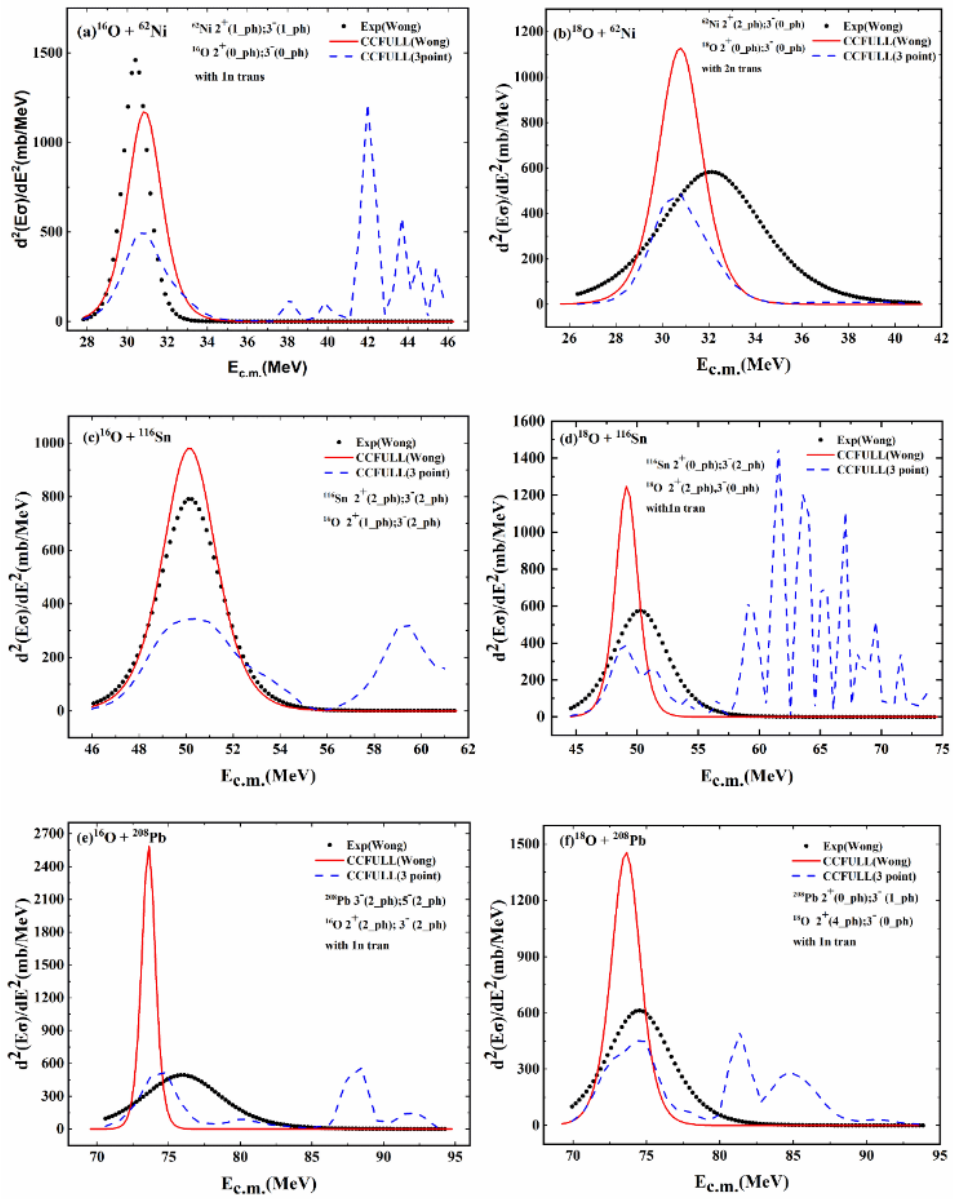

Figure 5: The black dots represent the experimental barrier distribution, obtained from the experimental fusion cross-sections using the second method (second derivative of Wong formula). The solid curve corresponds to the barrier distribution derived from the theoretical fusion cross-sections (CCFULL), also using the second method. The dashed line shows the barrier distribution extracted from the CCFULL theoretical cross-sections using the first method, i.e., the three-point difference formula. The experimental fusion cross-section for systems is come from [2, 39, 44].

Table 5: The experimental Coulomb barrier parameter of the systems was extracted from Wong's formula by fitting the experimental fusion cross-sections.

Systems	V_B^{exp} (MeV)	R_B^{exp} (fm)	$\hbar\omega_B$(MeV)
$^{16}O + ^{62}Ni$	30.42	27.68	2.59
$^{18}O + ^{62}Ni$	32.11	32.97	9.21
$^{16}O + ^{116}Sn$	50.17	29.59	5.45
$^{18}O + ^{116}Sn$	50.26	32.83	9.25
$^{16}O + ^{208}Pb$	75.96	33.86	11.48
$^{18}O + ^{208}Pb$	74.51	33.89	9.25

4. Conclusions

A rigorous analysis of nuclear structure and fusion dynamics in ^{16}O and ^{18}O with medium-heavy targets (^{62}Ni, ^{116}Sn, ^{208}Pb) is studied. CCFULL calculations with BW 91 proximity potentials show better agreement with experimental data. CCFULL calculations provide that multipole excitation of vibration states, phonon excitation, neutron transfer, and negative *Q*-value significantly enhance sub-barrier fusion cross-section. On the other hand, the incorporation of oxygen isotope ^{18}O influenced the enhancement of the studied systems. The findings of this investigation are as follows: The isotope ^{18}O, classified as neutron-rich, has a significant effect on the increase of the sub-barrier fusion cross-sections, in particular for systems with medium-heavy or heavy targets. An increase in fusion is due to the combined action of the neutron transfer (even if the *Q*-value is negative) and the correlations of vibrational couplings. Such observations underscore the necessity of performing comparisons between different targets with similar experimental conditions to determine the influence of the structural differences of the projectiles (^{16}O vs ^{18}O) on the dynamics of nuclear fusion. The oxygen isotope ^{18}O has a significant impact on predicting the main peak of the experimental barrier and broadening the coupling energy regions in the studied fusion systems, except in the ^{18}O + ^{208}Pb system. The fusion system can be improved by using a specific isotope for projectiles, as previously mentioned, except for those that utilize halo isotope projectiles (radioactive beams) [45].

Acknowledgements

The authors acknowledge the support for this study from the Department of Physics, College of Science, University of Sulaimani, Sulaymaniyah City, Iraq. We want to thank Dr. Aziz H. Fattah and Dr. Fouad A. Majeed for their support during our programming modifications.

Conflict of Interest

Authors declare that they have no conflict of interest.

References

1. S. Sinha, M.R. Pahlavani, R. Varma, R.K. Choudhury, B.K. Nayak, and A. Saxena, Phys. Rev. C **64**, 024607 (2001). https://doi.org/10.1103/PhysRevC.64.024607.
2. N.K. Deb, K. Kalita, H.A. Rashid, S. Nath, J. Gehlot, N. Madhavan, R. Biswas, R.N. Sahoo, P.K. Giri, A. Das, T. Rajbongshi, A. Parihari, N.K. Rai, S. Biswas, Khushboo, A. Mahato, B.J. Roy, A. Vinayak, and A. Rani, Phys. Rev. C **102**, 034603 (2020). https://doi.org/10.1140/epja/s10050-023-01168-4.
3. M.S. Gautam, R.P. Chahal, S. Duhan, and H. Khatri, in *DAE-BRNS Symposium on Nuclear Physics*, Guwahati, India, 2022, edited by Cotton University, p. 2.
4. G. Montagnoli, and A.M. Stefanini, Eur. Phys. J. A **53**, 169 (2017). https://doi.org/10.1140/epja/i2017-12350-2.
5. S.G. Steadman, and M.J. Rhoades-Brown, Annu. Rev. Nucl. Part. Sci **36**, 649 (1986). https://doi.org/10.1146/annurev.ns.36.120186.003245.
6. K. Hagino, N. Rowley, and A.T. Kruppa, Comput. Phys. Commun **123**, 143 (1999). https://doi.org/10.1016/S0010-4655(99)00243-X.
7. M.S. Gautam, H. Khatri, and K. Vinod, Nucl. Phys. A **984**, 9 (2019). https://doi.org/10.1016/j.nuclphysa.2019.01.002.
8. P. Jisha, A.M. Vinodkumar, S. Sanila, K. Arjun, B.R.S. Babu, J. Gehlot, S. Nath, N. Madhavan, R. Biswas, and A. Parihari, Phys. Rev. C **105**, 054614 (2022). https://doi.org/10.1103/PhysRevC.105.054614.
9. H. Esbensen, and S. Landowne, Phys. Rev. C **35**, 2090 (1987). https://doi.org/10.1103/PhysRevC.35.2090.
10. T. Rajbongshi, and K. Kalita, Cent. Eur. J. Phys **12**, 433 (2014). https://doi.org/10.1103/PhysRevC.35.2090.

11. T. Rajbongshi, K. Kalita, S. Nath, J. Gehlot, T. Banerjee, I. Mukul, R. Dubey, N. Madhavan, C.J. Lin, and A. Shamlath, Phys. Rev. C **93**, 054622 (2016). https://doi.org/10.1103/PhysRevC.93.054622.
12. K. Hagino, and N. Takigawa, Prog. Theor. Phys **128**, 1061 (2012). https://doi.org/10.1143/PTP.128.1061.
13. M. Beckerman, Rep. Prog. Phys **51**, 1047 (1988). https://doi.org/10.1088/0034-4885/51/8/001.
14. A.M. Stefanini, D. Ackermann, L. Corradi, D.R. Napoli, C. Petrache, P. Spolaore, P. Bednarczyk, H.Q. Zhang, S. Beghini, and G. Montagnoli, Phys. Rev. Lett **74**, 864 (1995). https://doi.org/10.1103/PhysRevLett.74.864.
15. C.R. Morton, A.C. Berriman, M. Dasgupta, D.J. Hinde, J.O. Newton, K. Hagino, and I.J. Thompson, Phys. Rev. C **60**, 044608 (1999). https://doi.org/10.1103/PhysRevC.60.044608.
16. V. Ghanghas, R.P. Chahal, S. Duhan, H. Khatri, and M.S. Gautam, Braz. J. Phys **52**, 84 (2022).
17. S. Rana, M. Bhuyan, R. Kumar, and B.V. Carlson, Phys. Rev. C **110**, 024601 (2024). https://doi.org/10.1103/PhysRevC.110.024601.
18. J.R. Leigh, M. Dasgupta, D.J. Hinde, J.C. Mein, C.R. Morton, R.C. Lemmon, J.P. Lestone, J.O. Newton, H. Timmers, and J.X. Wei, Phys. Rev. C **52**, 3151 (1995). https://doi.org/10.1103/PhysRevC.52.3151.
19. J.D. Bierman, P. Chan, J.F. Liang, M.P. Kelly, A.A. Sonzogni, and R. Vandenbosch, Phys. Rev. Lett **76**, 1587 (1996). https://doi.org/10.1103/PhysRevLett.76.1587.
20. C.R. Morton, M. Dasgupta, D.J. Hinde, J.R. Leigh, R.C. Lemmon, J.P. Lestone, J.C. Mein, J.O. Newton, H. Timmers, and N. Rowley, Phys. Rev. Lett **72**, 4074 (1994). https://doi.org/10.1103/PhysRevLett.72.4074.
21. M. Dasgupta, D.J. Hinde, J.R. Leigh, and K. Hagino, Nucl. Phys. A **630**, 78 (1998). https://doi.org/10.1016/S0375-9474(97)00745-8.
22. N. Rowley, G.R. Satchler, and P.H. Stelson, Phys. Lett. B **254**, 25 (1991). https://doi.org/10.1016/0370-2693(91)90389-8.
23. A.J. Najim, F.A. Majeed, and K.H. Al-Attiyah, in *IOP Conference Series: Materials Science and Engineering*, **571**, 012124 (2019). http://dx.doi.org/10.1088/1757-899X/571/1/012124
24. R. Gharaei, A. Fuji, and B. Azadegan, Chin. Phys. C **45**, 124101 (2021). https://doi.org/10.1088/1674-1137/ac23d3.
25. N. Chauhan and S.S. Godre, in *Proceedings of the DAE-BRNS Symposium on Nuclear Physics, 2018*, p. 618.
26. C.Y. Wong, Phys. Rev. Lett **31**, 766 (1973). http://dx.doi.org/10.1103/PhysRevLett.31.766.
27. W. Reisdorf, J Phys G: Nucl. Part. Phys **20**, 1297 (1994). http://dx.doi.org/10.1088/0954-3899/20/9/004.
28. I. Dutt, and R.K. Puri, Phys. Rev. C **81**, 064609 (2010). https://doi.org/10.1103/PhysRevC.81.064609.
29. A. Winther, Nucl. Phys. A **594**, 203 (1995). https://doi.org/10.1016/0375-9474(95)00374-A .
30. T. Rumin, K. Hagino, and N. Takigawa, Phys. Rev. C **61**, 014605 (1999). https://doi.org/10.1103/PhysRevC.61.014605.
31. C.Y. Wong, Phys. Lett. B **42**, 186 (1972). https://doi.org/10.1103/PhysRevLett.31.766 .
32. F.A. Majeed, R.S. Hamodi, and F.M. Hussian, J. Comput. Theor. Nanosci **14**, 2242 (2017). https://doi.org/10.1166/jctn.2017.6816.
33. M.Dasgupta, D.J.Hinde, N.Rowley, and A.M.Stefanini, Annu. Rev **48**, 401 (1998). https://doi.org/10.1146/annurev.nucl.48.1.401.
34. G. Zhang, X. Liu, and C. Lin, Phys. Rev. C **89**, (2014).
35. V. Tripathi, L.T. Baby, J.J. Das, P. Sugathan, N. Madhavan, A.K. Sinha, P.V. Madhusudhana Rao, S.K. Hui, R. Singh, and K. Hagino, Phys. Rev. C **65**, 014614 (2001). https://doi.org/10.1103/PhysRevC.65.014614.
36. M. Schramm, K.H. Maier, M. Rejmund, L.D. Wood, N. Roy, A. Kuhnert, A. Aprahamian, J. Becker, M. Brinkman, D.J. Decman, E.A. Henry, R. Hoff, D. Manatt, L.G. Mann, R.A. Meyer, W. Stoeffl, G.L. Struble, and T.F. Wang, Phys. Rev. C **56**, 1320 (1997). https://doi.org/10.1103/PhysRevC.56.1320.
37. R.H. Spear, At. Data. Nucl. Data. Tables **42**, 55 (1989).
38. D.K. McDaniels, J. Lisantti, I. Bergqvist, L.W. Swenson, X.Y. Chen, D.J. Horen, F.E. Bertrand, E.E. Gross, C. Glover, R. Sayer, B.L. Burks, O. Häusser, and K. Hicks, Nucl. Phys. A **467** 557 (1987). https://doi.org/10.1016/0375-9474(87)90386-1.
39. V.Y. Denisov, and I.Y. Sedykh, Eur. Phys. J. A **55**, 153 (2019). https://doi.org/10.1140/epja/i2019-12855-6.
40. N. Deb, K. Kalita, A. Rashid, A. Das, S. Nath, J. Gehlot, N. Madhavan, R. Biswas, R. Sahoo, P. Giri, A. Parihari, N. Rai, S. Biswas, A. Mahato, and B. Roy, Phys. Rev. C **105**, (2022). https://doi.org/10.1103/PhysRevC.105.054608.
41. M.S. Gautam, Chin. Phys. C **39**, 114102 (2015). https://doi.org/10.1088/1674-1137/39/11/114102.

42. D.C. Rafferty, M. Dasgupta, D.J. Hinde, C. Simenel, E.C. Simpson, E. Williams, I.P. Carter, K.J. Cook, D.H. Luong, S.D. McNeil, K. Ramachandran, K. Vo-Phuoc, and A. Wakhle, Phys. Rev. C **94**, 024607 (2016).
43. N. Deb, A. Rashid, A. Das, and K. Kalita, in *Proceedings of the DAE Symp. on Nucl. Phys. 65*, 2021.
44. R. Gharaei, A. Hadikhani, and V. Zanganeh, Nucl. Phys. A **990**, 47 (2019). https://doi.org/10.1016/j.nuclphysa.2019.06.003
45. C. Signorini, A. Yoshida, Y. Watanabe, D. Pierroutsakou, L. Stroe, T. Fukuda, M. Mazzocco, N. Fukuda, Y. Mizoi, M. Ishihara, H. Sakurai, A. Diaz-Torres, and K. Hagino, *Nucl. Phys. A* **735**, 329 (2004). https://doi.org/10.1016/j.nuclphysa.2004.02.015.

نهج مختلف: دور قطبية نظائر الأكسجين وديناميكيات الاقتران في تعزيز الاندماج تحت الحاجز

لينا صلاح الدين عبدالمجيد[1] وعادل محمد حسين[1]
[1] قسم الفيزياء، كلية العلوم، جامعة السليمانية، السليمانية، العراق

الخلاصة

يبحث هذا العمل بشكل منهجي في تعزيز الاندماج تحت الحاجز في التفاعلات المُستحثة بالأكسجين، مُسلِّطًا الضوء على الأدوار الجديدة لبنية المقذوفات وديناميكيات القنوات المقترنة. نُبيّن أن التوافق بين التوقعات النظرية والبيانات التجريبية يتحسَّن بشكل كبير من خلال الاهتزازات متعددة الأقطاب، وإثارات متعددة الفونونات، ونقل النيوترونات بقيم Q سالبة، باستخدام جهدي BW 91 وAW 95. بخلاف الدراسات السابقة، يُفسِّر هذا العمل تعزيز الاندماج تحت الحاجز المعتمد على النظائر عبر مناطق كتلة مختلفة من خلال الجمع بين جهدي BW 91 وAW 95 وإثارات متعددة الفونونات وقنوات نقل نيوترونية ذات قيم Q سالبة. بالنسبة للأنظمة $^{16,18}O + {}^{62}Ni,\ ^{116}Sn,$ and ^{208}Pb . تُحسَب دوال إثارة الاندماج وتوزيعات الحاجز باستخدام صيغة Wong وشيفرة CCFULL مُعَدَّلة. يُسهّل فائض النيوترونات في ^{18}O قنوات نقل نيوترونية ذات قيمة Q سالبة محددة، مما يُسهم في خفض حاجز الاندماج وتعزيز الاندماج تحت الحاجز. يُظهر تحليل توزيع الحاجز الدور الحاسم للبنية النووية في تحديد مشهد احتمالية الاندماج، ويُعدّ بمثابة تقنية مرجعية لتقييم الحسابات النظرية. نتج عن تفاعل $^{116}Sn + {}^{18}O$ قصدير قيمة مقطع عرضي محسوبة تضاعفت مقارنةً بنظام $^{116}Sn + {}^{16}O$. وبالمثل، فإن المقطع العرضي للاندماج $^{208}Pb + {}^{18}O$ أعلى من مقطع $^{208}Pb + {}^{16}O$ ، تم ملاحظة معدل مماثل للقذيفة ^{18}O، مما أدى إلى توسيع عرض الطاقة لتوزيع الحاجز بالمقارنة مع النتائج من القذيفة ^{16}O.

الكلمات المفتاحيه: تعزيز اندماج الحواجز الفرعية، نظائر المشروع، نقل النيترونات، تعديل القنوات المرتبطة، جهد القرب (BW 91 AW 95).